Heat-Mediated Micro- and Nano-Pore Evolution in Sea Urchin Biominerals

Marie Albéric[1], Emil Zolotoyabko[2], Oliver Spaeker[3], Chenghao Li[3], Maryam Tadayon[4], Clemens Schmitt[3], Yael Politi[4], Luca Bertinetti[4] and Peter Fratzl[3]

[1]Sorbonne Université, Laboratoire Chimie de la Matière Condensée de Paris, 75005 Paris, France
[2]Department of Materials Science and Engineering, Technion-Israel, Institute of Technology, 32000 Haifa, Israel
[3]Department of Biomaterials, Max Planck Institute of Colloids and Interfaces, 14476 Potsdam, Germany

[4]Technische Universität Dresden - Center for Molecular and Cellular Bioengineering, 01307 Dresden, Germany

SUPPLEMENTARY INFORMATION

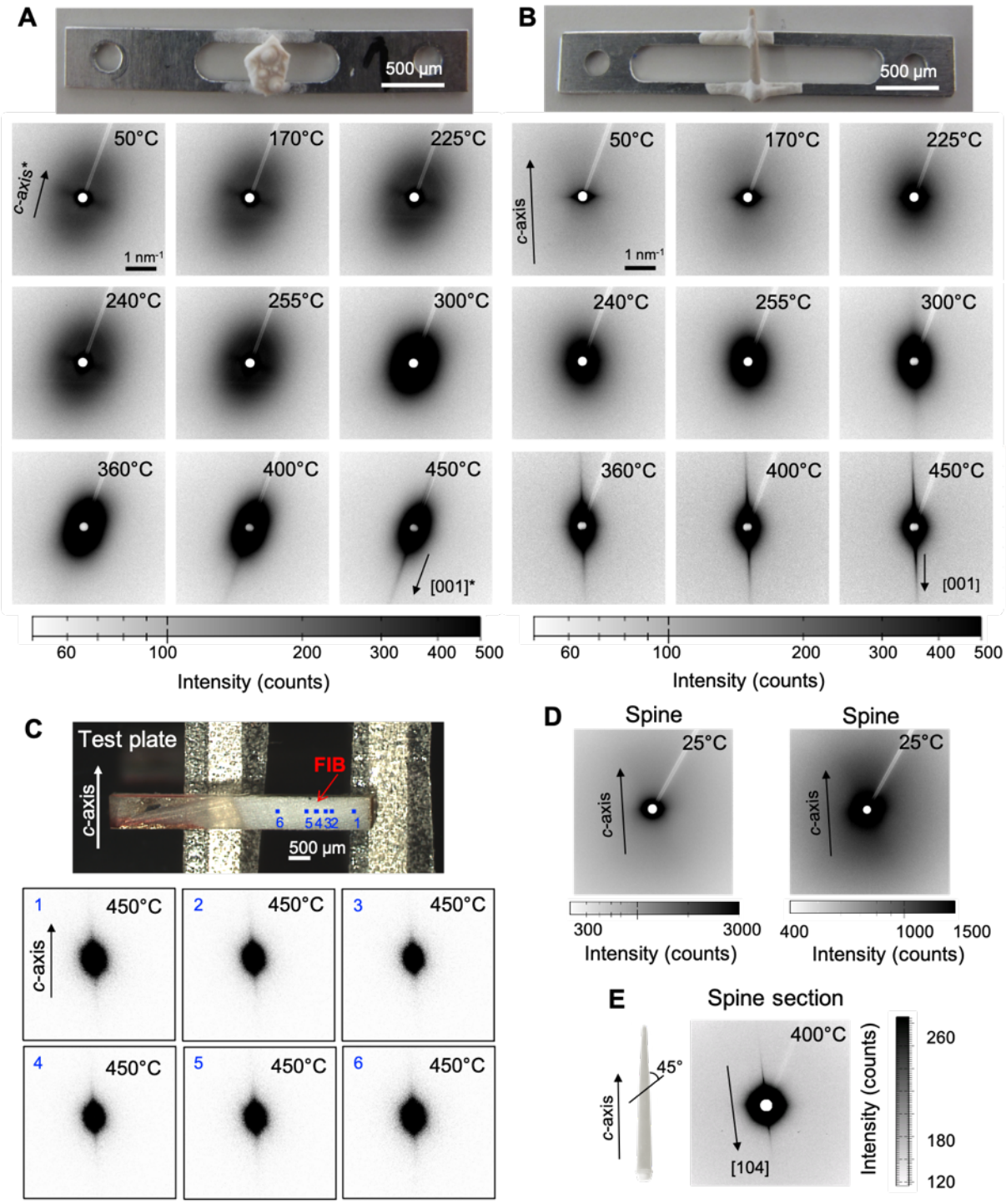

Figure SI1. Selected *in situ* 2D SAXS patterns for the azimuthal integration presented in Figure 6 of A) the test plate and B) the spine sample. The photographs of the samples are shown after the *in situ* SAXS measurements. (*) orientation of the *c*-axis and the [001]-direction determined according to laboratory SAXS measurements C) 450°C pre-annealed test plate sample used for FIB experiment, the localization of the analyzed FIB volume is indicated. The SAXS laboratory results show that the streak is oriented parallel to the c-axis. 2D SAXS patterns of D) a native spine with its *c*-axis perpendicular to the beam with two different scales for the scattered intensity and E) 400°C pre-annealed spine sectioned at 45° to its *c*-axis showing the streak in the [104]-direction. Note that the electron density inhomogeneities in biominerals that lead to the measured SAXS contrast could be ACC inclusions and/or hydrated organic macromolecules, the latter becoming occluded during the growth of biominerals. Regarding ACC inclusions, we note that nanodomains in biogenic calcite, tens of nm in size, indeed are observed after ACC crystallization (see, e.g.[1,2]), which is characteristic for the non-classical crystal growth by amorphous particles attachment and subsequent crystallization[1,3]. However, our pristine samples contain anhydrous ACC, which electron density is very close to that in calcite[4,5] and, then, cannot significantly influence the SAXS signals. Therefore, we suggest that at the pristine stage, the nano-pores are filled of hydrated organics rather than ACC.

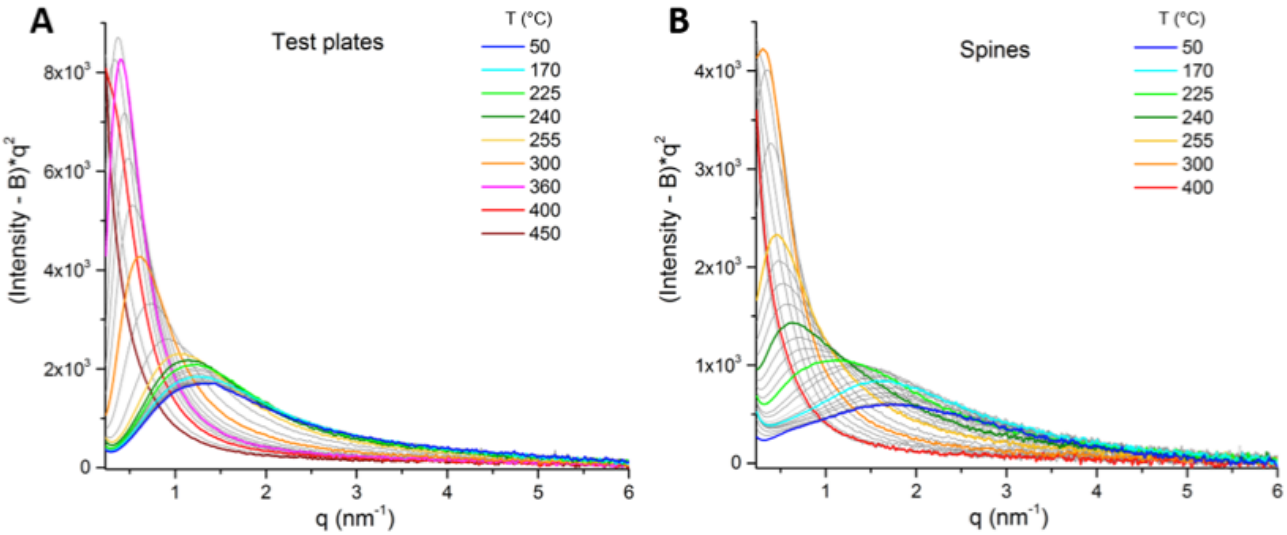

Figure SI2. Kratky plots of the SAXS data for A) the test plates and B) the spines.

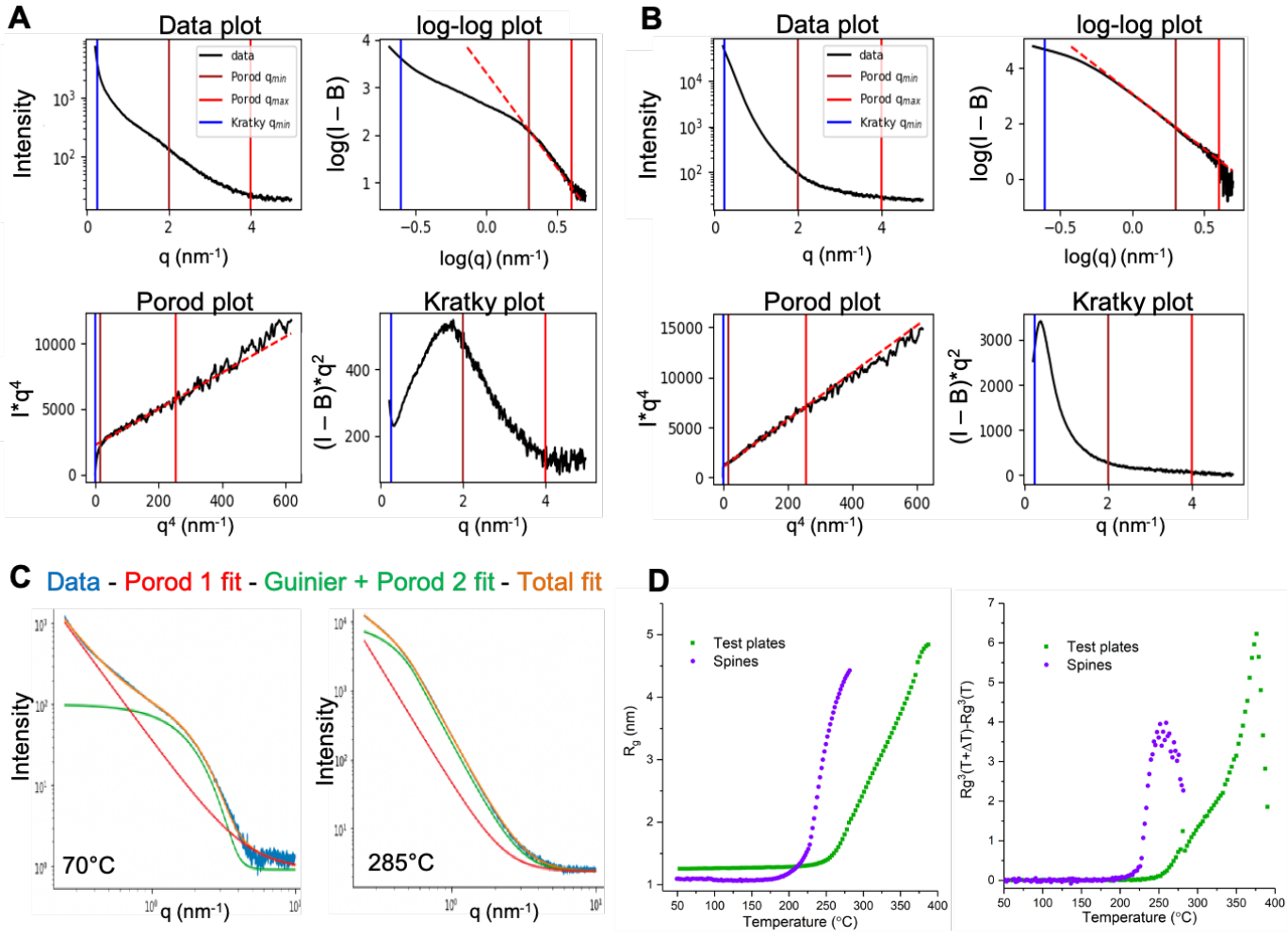

Figure SI3.

T parameter (T_p) analysis for the spine sample annealed at: A) 50°C and B) 275°C; the different plots needed for the T_p analysis are displayed. C) R_g analysis for the spine sample annealed at 70°C and 285°C; I_{meas}, the Porod 1 fit at low q, the Guinier + Porod 2 fit at higher q and the total fit are displayed.
D) R_g values up to 280 °C and 390 °C for the spines and test plates, respectively and the corresponding temperature-dependent increments, $R_g^n(T + \Delta T) - R_g^n(T)$, for the spines and test plates for $n = 3$. The increments show a continuous growth followed by a sharp decrease respectively at 250°C and 370°C, for the spines and the test plates, which may correspond to organics destruction.

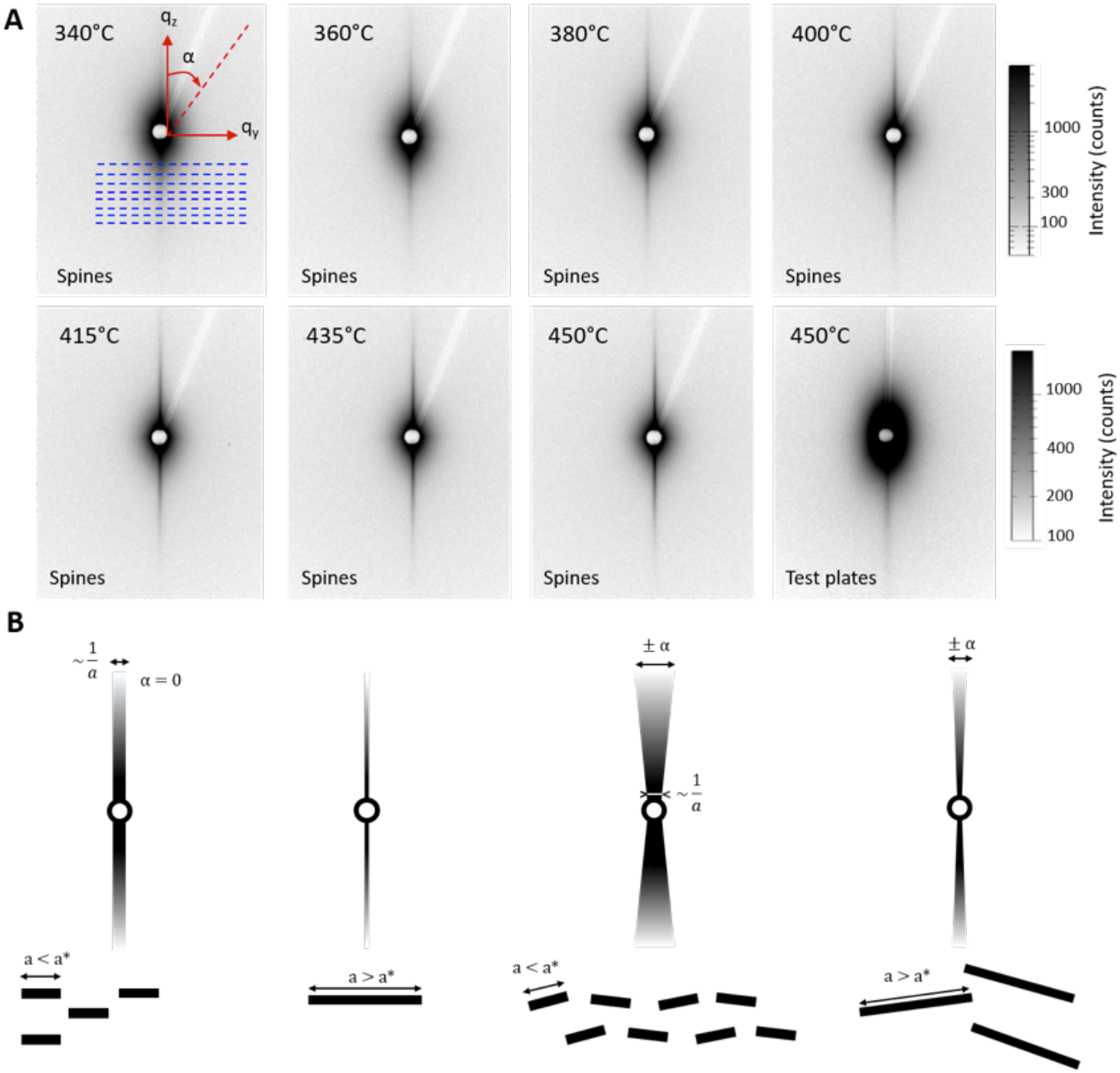

Figure SI4. [001]-streak analysis.

A) SAXS signals of an annealed spine from 340 °C to 450 °C measured for 1 s and SAXS signal of a 450 °C test plate measured for 2 s. In order to have vertical streaks, the SAXS signals were rotated 2° for the spine and 18° for the test plate with respect to the vertical of the image. The coordinate system defined with q_y perpendicular to the streak and q_z aligned with the streak is indicated.

B) Scheme showing the relation between the shape of the streaks and the size (a) and the angular spread (α) of the scattering surfaces. Four cases are presented: 1) when a<a* (a*, the maximum size of the surfaces detected by the μSpot set up ~ 100 nm) and α ~ 0, the width of the vertical streak is proportional to 1/a, 2) when a>a*, the streak is very thin and the size of the scattering interfaces cannot be calculated from the width of the streak, 3) when a<a* and α>0, the size of the surfaces can be calculated from the width of the streak at q=0, and is proportional to 1/a, and α informs on the degree of alignment (or misorientation) of the scattering surfaces and 4) when a>a* and α>0, only the degree of alignment of the scattering surfaces can be estimated.

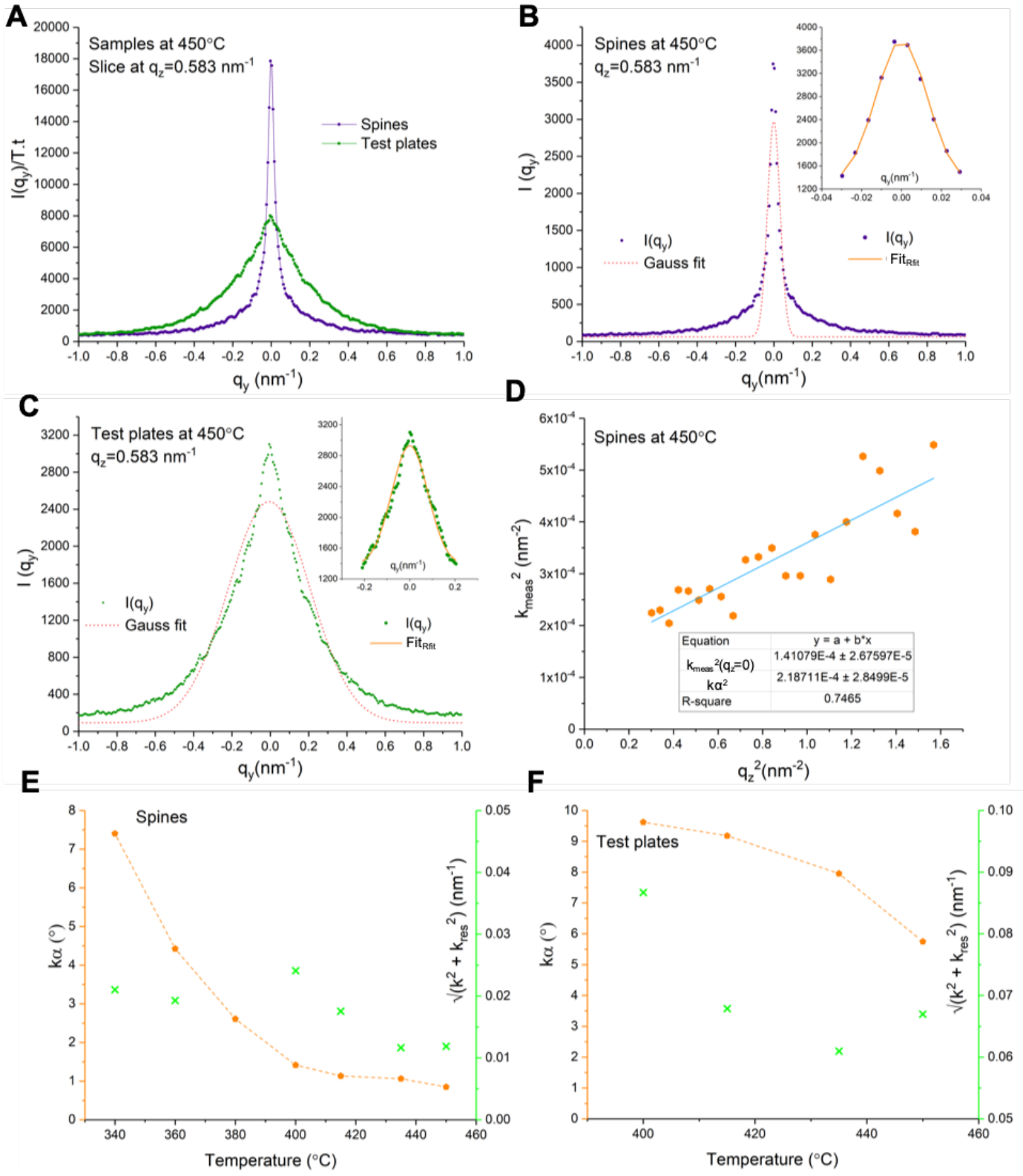

Figure SI5. [001]-streak analysis. A) measured scattering intensity across the streak of the 450°C annealed samples for q_z=0.583 nm^{-1} normalized by the measurement time (t) and the transmission of the sample (T), B-C) examples for the spine and test plate samples for q_z= 0.583 nm^{-1} of: 1) the Gaussian fit $\left(y_0 + \frac{A}{\sigma\sqrt{2\pi}} e^{-\frac{(x-x_0)}{\sigma^2}}\right)$ and 2) the fit, Fit$_{Rfit(z)}$ of the data with $I_{meas}(q_y) = y_1 + b \cdot e^{-\frac{1}{4}\cdot q_y^2 \cdot R_{fit(z)}^2}$, where $R_{fit(z)} = \frac{\sqrt{4\cdot ln2}}{k_{meas}}$ and k_{meas}, the half-width at half-maximum of $I_{meas}(q_y)$ across the streak. D) $k_{meas}^2(q_z^2)$ plot for 450°C spines, linearly fitted to obtain $k_{meas}(q_z=0)$, i.e. $\sqrt{k^2 + k_{res}^2}$ and k_α, the angular spread and E-F) $\sqrt{k^2 + k_{res}^2}$ and k_α plots as a function of the temperatures for the spine and test plate samples.

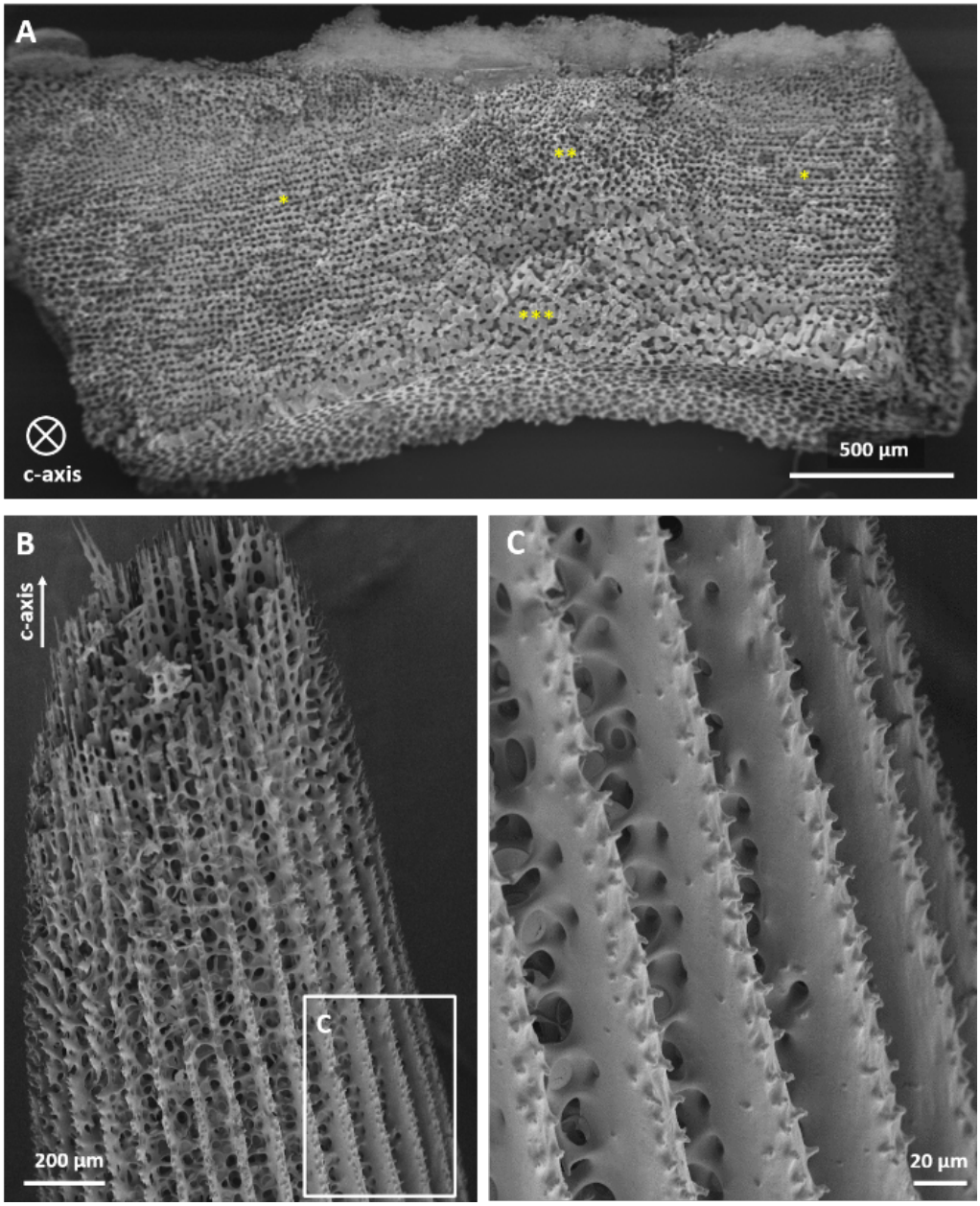

Figure SI6. A) Fractured section of an interambulacral test plate perpendicularly to its c-axis showing *galleried, ** labyrinthic and ***perforate stereom, B and C) SEM micrographs showing the forming septa of a growing spine by densification of the extremities of the radial laminar sheets of the stereom, which occurs from the periphery to the center of the spines, in agreement with Heatlfield 1971[6].

Table 1. Diameters of the pores and the struts of the different type of stereom in the test plates and the spines measured on SEM micrographs.

	Stereom type	Pore diameter (µm)	Struts diameter (µm) Septa width (µm)
Interambulacral plate	Labyrinthic	10 - 20	8 - 12
	Galleried	5 - 10	8 - 10
	Perforate	15 - 25	20 - 30
Middle of the spine	Labyrinthic	5 - 15	5 - 10
	Laminar	8 - 25	5 - 8
	Imperforate (septa)	-	60 - 70

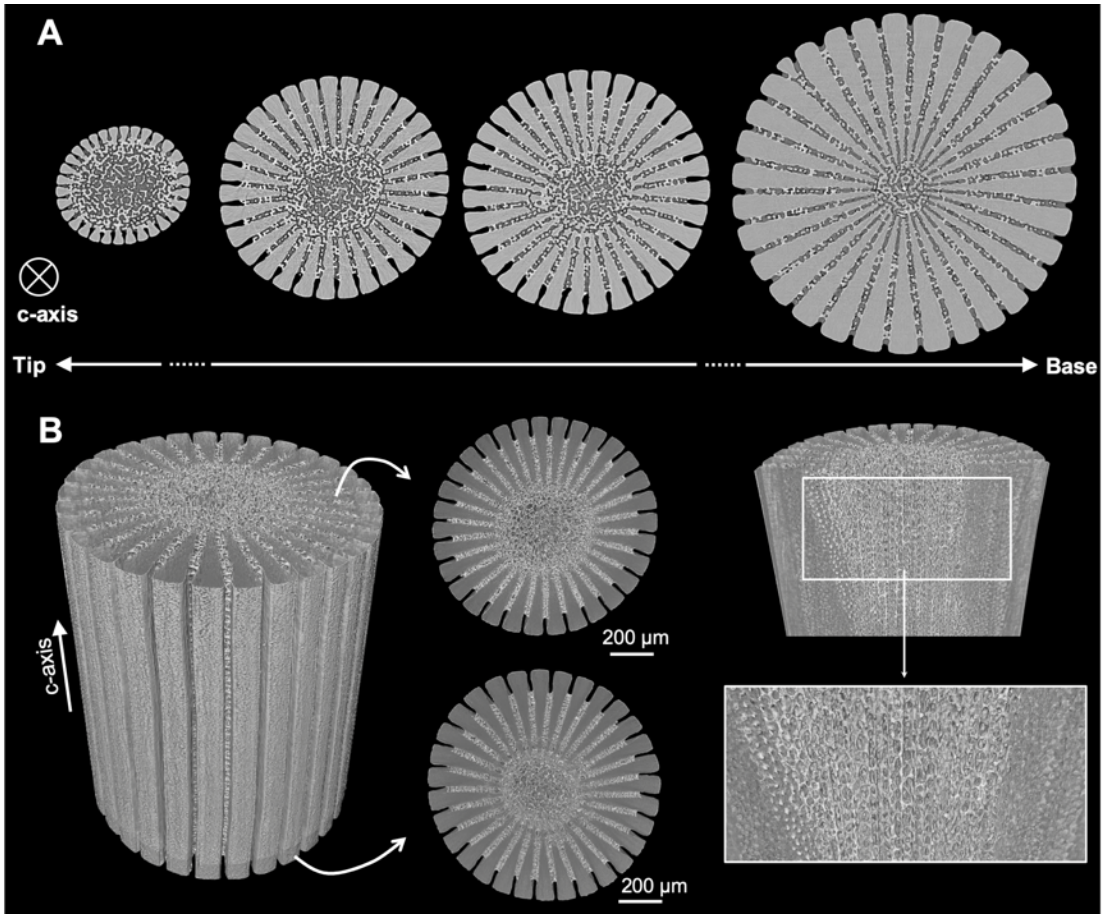

Figure SI7. CT data of a sea urchin spine. A) CT virtual sections perpendicular to the calcite c-axis from tip (left) to base (right) and B) 3D visualization of the CT data of the volume analyzed in the middle of the spine obtained with the rendered volume function of the 3D Amira (FEI) software.

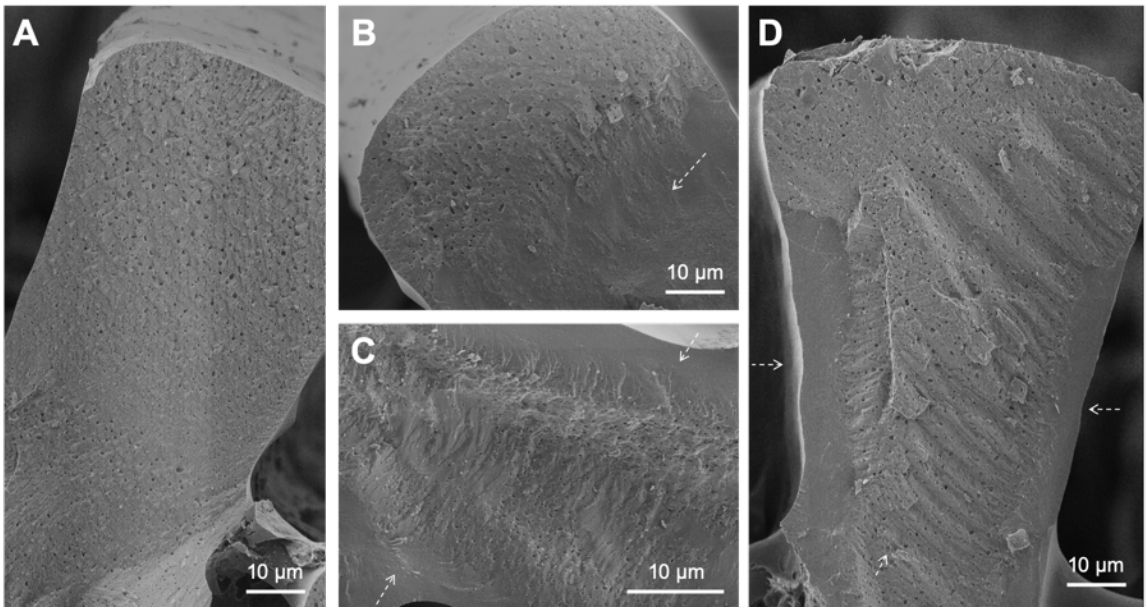

Figure SI8. SEM micrographs of fractured sections of sea urchin spines annealed previously at A and B) 350°C, C) 300°C and D) 400°C. The dashed arrows point the layers with no observable pores.

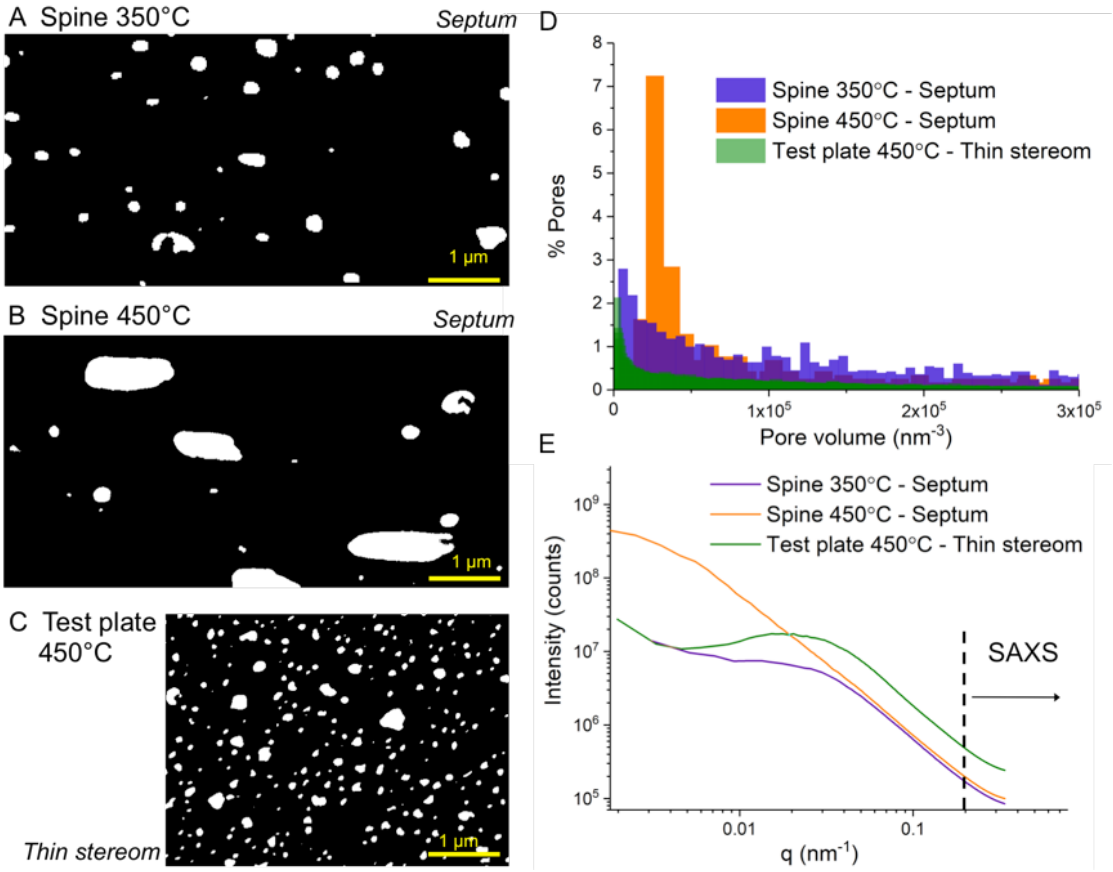

Figure SI9. Examples of threshold FIB-SEM micrographs with the pores represented in white of A) the septum of a spine annealed at 350 °C, B) the septum of a spine annealed at 450 °C and C) the thin stereom of a test plate annealed at 450 °C. D) Histograms of the volume of the pores and E) Azimuthal integrations of the Fourier transforms of the three annealed samples. The SAXS q range starts approximately (~ 0.2 nm^{-1}) where the FIB-SEM one finishes as indicated by the dashed line.

Table SI2. Results of the data analysis of the FIB-SEM measurements of the 350°C and 450°C spine and the 450°C test plate samples.

	Spine 350°C	Spine 450°C	Test plate 450°C
Measured volume (μm^3)	339	264	108
Number of pores	13738	2822	30799
Total pore volume (μm^3)	17	15	9
Density of pores (μm^{-3})	41	11	285
%Vol of pores	5.0	5.7	8.3
Min pore volume (nm^3)	6170	12890	805
Min diameter (if spherical pores) (nm)	23	29	12
Min c dimension (if ellipsoidal pores with a=b and c=2a) (nm)	36	46	18
Max pore volume (um^3)	0.12	2.20	0.02
Max diameter (if spherical pores) (nm)	612	1614	348
Max c dimension (if ellipsoidal pores with a=b and c=2a) (nm)	972	2562	552

(1) Cölfen, H.; Antonietti, M. *Mesocrystals and Nonclassical Crystallization*; Wiley: New York, 2008.
(2) Schmidt, I.; Lee, K.; Zolotoyabko, E.; Werner, P.; Shim, T. S.; Oh, Y. K.; Fratzl, P.; Wagermaier, W. Nanocrystalline Calcitic Lens Arrays Fabricated by Self-Assembly Followed by Amorphous-to-Crystalline Phase Transformation. *ACS Nano* **2014**, *8* (9), 9233–9238. https://doi.org/10.1021/nn503015c.
(3) De Yoreo, J. J.; Gilbert, P. U. P. A.; Sommerdijk, N. A. J. M.; Penn, R. L.; Whitelam, S.; Joester, D.; Zhang, H.; Rimer, J. D.; Navrotsky, A.; Banfield, J. F.; Wallace, A. F.; Michel, F. M.; Meldrum, F. C.; Cölfen, H.; Dove, P. M. Crystallization by Particle Attachment in Synthetic, Biogenic, and Geologic Environments. *Science* **2015**, *349* (6247), aaa6760. https://doi.org/10.1126/science.aaa6760.
(4) Jensen, A. C. S.; Imberti, S.; Parker, S. F.; Schneck, E.; Politi, Y.; Fratzl, P.; Bertinetti, L.; Habraken, W. J. E. M. Hydrogen Bonding in Amorphous Calcium Carbonate and Molecular Reorientation Induced by Dehydration. *J. Phys. Chem. C* **2018**, *122* (6), 3591–3598. https://doi.org/10.1021/acs.jpcc.7b10459.
(5) Saharay, M.; Yazaydin, A. O.; Kirkpatrick, R. J. Dehydration-Induced Amorphous Phases of Calcium Carbonate. *J Phys Chem B* **2013**, *117* (12), 3328–3336. https://doi.org/10.1021/jp308353t.
(6) Heatfield, B. M. Growth of Calcareous Skeleton during Regeneration of Spines of Sea Urchin, Strongylocentrotus-Purpuratus (Stimpson) - Light and Scanning Electron Microscopic Study. *J. Morphol.* **1971**, *134* (1), 57–90. https://doi.org/10.1002/jmor.1051340105.